Received 7 September 2023; accepted 21 September 2023. Date of publication 26 September 2023; date of current version 17 October 2023.

Digital Object Identifier 10.1109/OJCOMS.2023.3319041

Measuring the Impact of Beamwidth and Bandwidth on the Wide-Sense Stationarity of Millimeter-Wave Channels

ANMOL BHARDWAJ [1,2], JACK CHUANG [1], CAMILLO GENTILE [1] (Member, IEEE), AND CHIEHPING LAI [1]

[1] Radio Access and Propagation Metrology Group, National Institute of Standards and Technology, Gaithersburg, MD 20899, USA
[2] Department of Chemistry and Biochemistry, University of Maryland at College Park, College Park, MD 20742, USA

CORRESPONDING AUTHOR: C. GENTILE (e-mail: camillo.gentile@nist.gov)

ABSTRACT If a wireless channel is said wide-sense stationary (WSS), the mean and autocorrelation of its small-scale fading are position invariant. This occurs when the channel is rich in propagation paths – their complex summation averages out any position-specific characteristics. Extensive measurement campaigns have validated the microwave channel to be WSS – it is inherently rich in diffracted paths, the 1G to 4G systems that operate there employ omnidirectional antennas which detect paths from all directions, and the systems feature narrow bandwidths which sum paths over long sample periods. Popular millimeter-wave (mmWave) channel models assume the channel is WSS without measurement-based validation even though the channel is inherently sparse due to weak diffraction, and the 5G systems that operate there employ pencilbeam antennas and feature ultrawide bandwidths. In fact, a recent measurement campaign showed the 60 GHz channel is non-WSS at narrow beamwidths and wide bandwidths, however the campaign considered only one measured channel and only a *discrete* set of beamwidths and bandwidths. For comprehensive analysis, in this paper we measured 88 channels over three indoor and two outdoor environments with our 60 GHz channel sounder and varied the beamwidth and bandwidth *continuously* to find the crossover points when the channel transitions from WSS to non-WSS.

INDEX TERMS 60 GHz, mmWave, fast fading, small-scale fading.

I. INTRODUCTION

SMALL-SCALE fading refers to fluctuation in the magnitude of the channel response that results from the complex summation of propagation paths. Specifically, as the transmitter (TX), receiver (RX), or any ambient scatterers move, the path lengths change, effecting oscillation in their phase and in turn positive and negative wave interference. Since the fading occurs over the displacement of just wavelengths, it is often referred to as fast fading. When many paths are detected, the complex summation averages out the displacement-specific characteristics, yielding a channel that is wide-sense stationary (WSS), for which the mean and autocorrelation of its small-scale fading are displacement[1] invariant. The assumption of wide-sense stationarity in popular channel models for 1G to 4G systems, which operate in the microwave bands, has been validated through extensive measurement [9], [10], [11], [12]. Unfortunately, the assumption was ported to 5G models [13], [14], [15], [16], [17], [18], [19] even for new millimeter-wave (mmWave) bands without such validation; in fact, a recent measurement campaign at 60 GHz by Iqbal has demonstrated otherwise [4], [5].

There are three main reasons why the microwave channel is WSS and the mmWave channel may not be. Firstly, the mmWave channel is inherently sparse due to weak diffraction [20], [21], so fewer paths will be detected in the complex summation [4], [20], [22]. Secondly, to compensate for the greater pathloss at mmWave, systems will employ directional antennas with beamwidths on the order of degrees – so-called *pencilbeams* – thanks to their high gains. The pencilbeams act as spatial filters, significantly attenuating paths that fall outside the beamwidth, reducing yet further the detected paths. Finally, 5G bandwidths will

1. Some papers express small-scale fading as a function of time rather than displacement [1], [2], [3]. In reality, small-scale fading arises from displacement of the TX, RX, or any ambient scatterers, which happens to manifest itself over time as well. But without displacement, there would be no small-scale fading and so measuring it over time in this case would be incorrect. As such, in this paper we measure it by varying displacement, as other papers do [4], [5], [6], [7], [8].

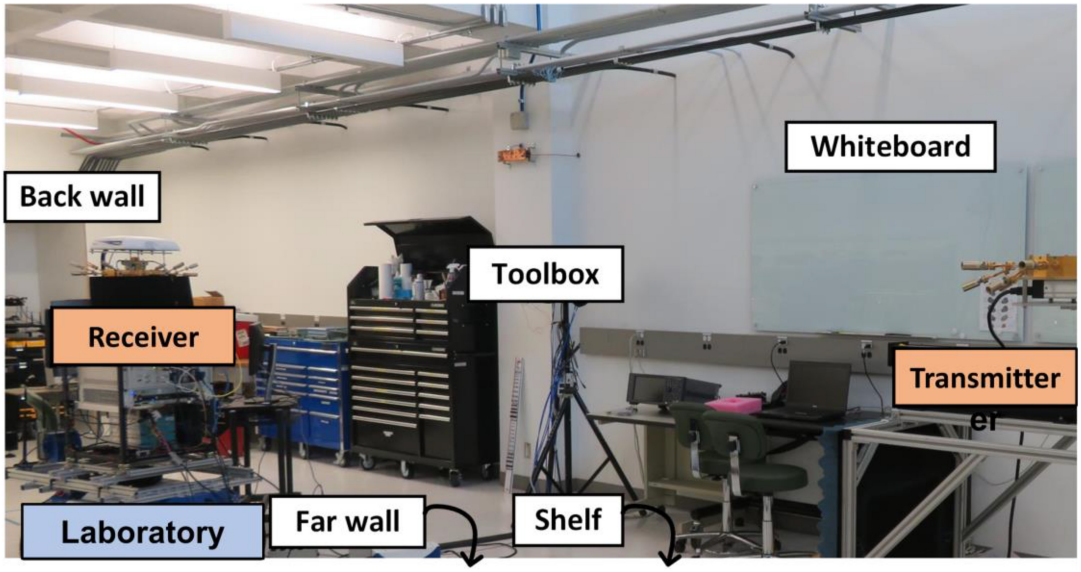

FIGURE 1. Photograph of the transmitter and receiver (labeled in orange) of our 60 GHz 3D double-directional switched-array channel sounder collecting measurements in a Laboratory environment. Some of the persistent scatterers detected in the environment are labeled in white.

be on the order of hundreds or even thousands – rather than tens – of MHz, so the RX sample period will increase drastically. Consequently, the number of paths arriving within a single delay sample will be significantly less [23].

The paper by Iqbal is of notable impact because, to our knowledge, there is no other measurement-based validation of mmWave wide-sense stationarity to date. Although the paper demonstrates a counterexample, it lacks comprehensive analysis: only three beamwidths (15°, 30°, and 360°) specific to the different channel sounders used for measurement were considered, yet mmWave antennas can have beamwidths as narrow as 3° [24]; analogously, only nine discrete bandwidths (from 10 MHz to 4 GHz) were considered. Finally, only one channel – from a single scatterer (a wall) in a single environment (a laboratory) – was considered.

To fill this void, in this paper we conduct a comprehensive analysis of mmWave wide-sense stationarity, implementing two significant improvements:

1. Rather than consider the channel measured from a single scatterer in a single environment, we consider the channel from 88 scatterers over three indoor and two outdoor environments measured with our high-precision 60 GHz 3D double-directional channel sounder;
2. Rather than analyzing only three *discrete* beamwidths and nine *discrete* bandwidths, we vary the beamwidth and bandwidth *continuously* – using the *same* channel sounder for more trustworthy results – and rather than rendering a binary decision of WSS or non-WSS for each combination, we compute the crossover beamwidth and crossover bandwidth when the channel transitions from WSS to non-WSS.

The rest of the paper is developed as follows: Section II describes our channel sounder and measurement campaign. In Section III, the measurements are processed into beamwidth- and bandwidth-dependent channel impulse responses, which are analyzed in Section IV to determine the crossover beamwidth and crossover bandwidth when the channel transitions from WSS to non-WSS; comprehensive results of the crossover points are also compiled in this section. The final section is reserved for conclusions.

II. CHANNEL MEASUREMENTS

Channel measurements were collected using our 60 GHz 3D double-directional switched-array channel sounder [25], pictured in Fig. 1. The RX features a spherical array of 16 scalar feed horn antennas with 22.5° beamwidth, together synthesizing a 360° field-of-view (FoV) in azimuth and 45° in elevation. The TX is almost identical except that it features a hemispherical array of only eight horns, limiting the azimuth FoV to 180°.

At the TX, an arbitrary waveform generator produces a repeating M-ary pseudorandom (PN) codeword with 0.5 ns chip duration, corresponding to 2 GHz bandwidth. The codeword is upconverted to precisely 60.5 GHz and then radiated by a horn. At the RX, the response received by a horn is downconverted back and then sampled at 40 Gsamples/s. Finally, the sampled response is matched filtered with the codeword to generate a complex-valued channel impulse response (CIR) as a function of delay. The codeword is electronically switched through each pair of TX and RX horns in sequence, resulting in 8 x 16 = 128 CIRs, which is referred to as an acquisition. An optical cable between the TX and RX is used for synchronous triggering and phase coherence. When factoring in TX power, antenna gains, codeword processing gain, system noise, and remaining components of the link budget, the maximum measurable path loss of the system is 162 dB.

TABLE 1. Environment traits.

Environment		Principal construction materials	Horizontal dimensions	Large-scale TX-RX distance	Number of paths per scenario (N*)		Number* of persistent paths per scenario
					Mean of N* (along rail)	Std. dev. of N* (along rail)	
Indoor	Laboratory	Metal cabinets and racks, drywall, marble floor	14 m x 7 m	4.4 m – 6.7 m	74.5	4.3	5.0
	Lobby	Wood wall panels, leather chairs, carpet	15 m x 10 m	9.6 m –10.1 m	24.9	2.4	4.8
	Lecture Room	Fabric wall panels, glass and wood doors, plastic chairs, carpet	19 m x 10 m	9.7 m –12.2 m	35.5	5.1	5.5
Outdoor	Pathway	Foliage, concrete buildings and walkways	91 m x 43 m	7.3 m – 15.1 m	11.1	1.5	3.8
	Courtyard	Metal cars and tables, concrete buildings and walkways	38 m x 23 m	6.0 m – 12.5 m	15.3	2.1	4.0

*Averaged over the four scenarios per environment

The 128 CIRs per acquisition are coherently combined through the SAGE super-resolution algorithm [26], [27] to extract channel paths and their properties. The output from SAGE for the acquisition at some displacement d is N channel paths indexed through n, together with path properties in a six-dimensional space: complex amplitude $\alpha_n(d)$, delay $\tau_n(d)$, and 3D double-directional angle $\boldsymbol{\theta}_n(d) = [\theta_n^{\mathrm{TX,A}}(d), \theta_n^{\mathrm{TX,E}}(d), \theta_n^{\mathrm{RX,A}}(d), \theta_n^{\mathrm{RX,E}}(d)]$, where TX, RX, A, and E denote angle-of-departure (AoD) from the TX, angle-of-arrival (AoA) to the RX, azimuth, and elevation, respectively.

Measurements were collected in three indoor environments – Laboratory, Lobby, and Lecture Room – and two outdoor environments – Pathway and Courtyard. The principal construction materials and the horizontal dimensions of the environments are shown in Table 1. In each environment, four scenarios with two *large-scale* TX locations and two large-scale RX locations were investigated, for a total of 20 scenarios altogether. The range of the large-scale distance between the TX and RX per environment are also shown in Table 1. Line-of-sight (LoS) conditions were maintained throughout. The TX was mounted on a fixed tripod at 1.6 m height. To measure small-scale fading by varying displacement, as is done in [4], [5], [6], [7], [8], the RX was mounted on a 90 cm rail (linear positioner) whose translation was parallel to the ground, also at 1.6 m height. The measurement per scenario consisted of 1801 channel acquisitions as the RX was translated, with *small-scale* displacement of 0.05 cm between each acquisition (ten samples per wavelength channel is WSS) indexed as $d = 0$ cm. . . 90 cm. It required about 30 minutes to capture all 1801 acquisitions, so static channel conditions were maintained for the whole duration (no pedestrian, vehicular motion, etc.). Fig. 2(a) shows the paths extracted from one acquisition in the Laboratory.

III. BEAMWIDTH- AND BANDWIDTH-DEPENDENT CIR

In Iqbal's work [5], the CIR was acquired by mechanically steering the TX and RX antennas towards a scatterer that was identified *a priori*. Out approach is similar, but instead of a single CIR, 128 CIRs were acquired and coherently combined to extract distinct channel paths. Synthetic antennas with variable beamwidth and a transmitted codeword with variable bandwidth were then applied to the extracted paths to *reconstruct* a beamwidth- and bandwidth- dependent CIR. The advantage of our approach is four-fold:

1) The synthetic antennas are steered towards persistent scatterers identified *a posteriori* from the acquisitions, rather than identifying presumptive scatterers *a priori*.
2) The synthetic antennas are constantly steered to realign with the angle of the scatterer as the RX moved along the rail, in contrast to alignment only at the first displacement on the rail (misalignment along the rail distorts the CIR due to antenna gain off boresight).
3) Rather than analyzing the wide-sense stationarity of just three discrete beamwidths (15°, 30°, 360°), we vary the beamwidth continuously from 360° down to 1° to determine the crossover beamwidth when the channel transitions from WSS to non-WSS;
4) Rather than analyzing the WSS of just nine discrete bandwidths (from 10 MHz to 4 GHz), we vary the bandwidth continuously from 10 MHz up to 2 GHz to determine the crossover bandwidth when the channel transitions from WSS to non-WSS.

In this section, we explain how to reconstruct the beamwidth- and bandwidth-dependent CIRs from the extracted paths.

A. PERSISTENT PATHS

Diffuse scattering at mmWave originates from ambient objects on the order of wavelengths in size – from objects that are inherently small, or from large objects with rough surfaces, with tiny intricacies, etc. The resultant diffuse paths tend to be weak – but numerous – collectively comprising up to 47% of the total received power [28], [29], [30]. Because they vary in path gain, delay, and angle over just fractions of a wavelength, the total number of paths N extracted in turn varies along the rail, despite a length of only 90 cm. Table 1 contains the mean and standard deviation of N along the rail per environment. The mean number is greater indoors due to more clutter (more scatterers); the Laboratory, in particular,

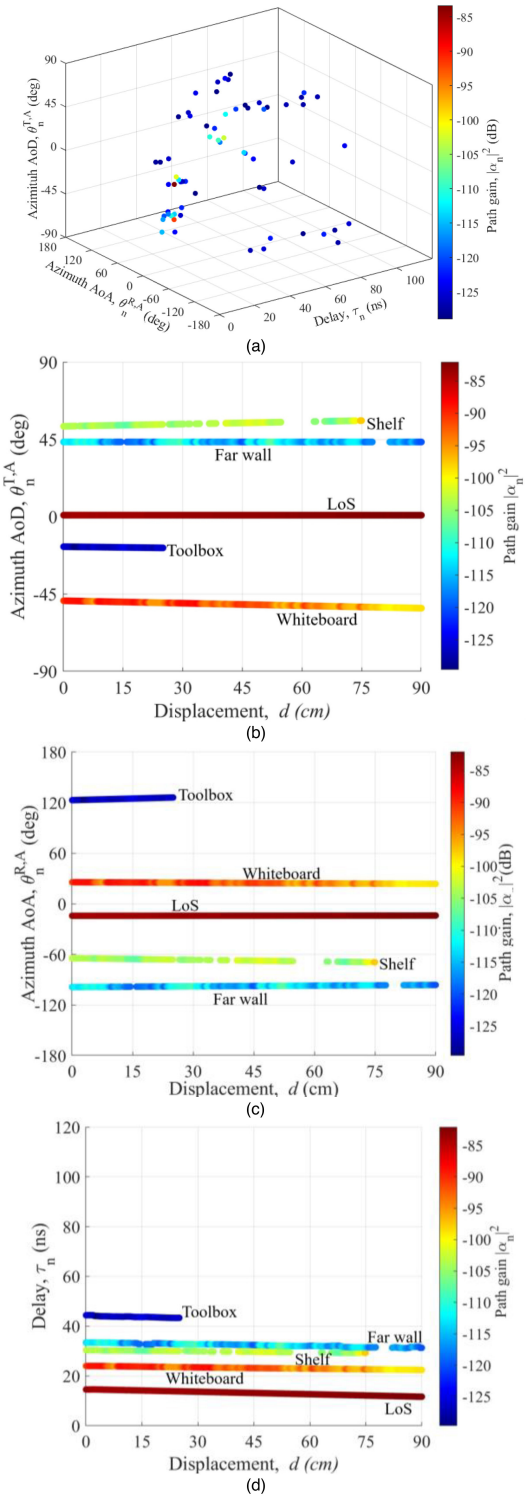

FIGURE 2. Channel paths extracted from a Laboratory scenario. (a) All paths are shown, at the first displacement (d = 0 cm) on the rail, displayed in azimuth AoD vs. azimuth AoA vs. delay. (b-d) Only persistent paths are shown, for all displacements (d = 0 cm…90 cm), labeled against the originating scatterers identified, displayed in (b) azimuth AoD vs. displacement, (c) azimuth AoA vs. displacement, and (d) delay vs. displacement.

is laden with metallic instruments. The mean number is also greater indoors due to less free-space loss by virtue of smaller dimensions (shorter path lengths), enabling detection of more diffuse paths, in turn giving rise to greater standard deviation. Outdoors, variation in the number of paths was caused mostly by obstruction and scattering from foliage but diffuse scattering from buildings was also observed.

In contrast to diffuse paths, specular paths from flat surfaces tend to be strong and *persistent* in path gain, delay, and angle along the rail, as is the LoS path. Given their desirable traits, these *persistent paths* – as we refer to them – are used here for beam steering. The technique to robustly identify and classify persistent paths is described in [31]. Fig. 2(b-d) display five persistent paths, identified from all the paths extracted from the Laboratory scenario in Fig. 2(a); the associated scatterers are labeled in Fig. 1. The persistent paths are displayed versus displacement to underscore how their azimuth AoD, azimuth AoA, and delay vary gradually along the rail. The paths vary up to a couple of degrees in AoD and AoA (and up to a couple nanoseconds in delay), highlighting the importance of constant realignment. The Toolbox, Whiteboard, Shelf, and Far Wall exhibit more variability as the reflected paths traverse their surfaces compared to the LoS path that simply propagate through air. The greater variability is due to their non-flat surfaces affecting angle and delay, and their composite materials affecting path gain. For example, the Toolbox's recessed face with highly reflective door handles can be observed in Fig. 1. Note also that some paths are not visible across the whole rail given their small dimensions, most notably the Toolbox. Table 1 also contains the average number of persistent paths per environment, which ranged between 3.8 and 5.5.

B. BANDWIDTH DEPENDENCE

Once all the persistent paths are identified, the next step is to reconstruct the bandwidth-dependent CIR. To that end, the spatial CIR of the channel per scenario is written as

$$h(d,\tau,\boldsymbol{\theta};B)=\sum_{n=1}^{N}\alpha_n(d)\cdot p\left(\frac{B}{2}\tau-\tau_n(d)\right)\cdot\delta(\boldsymbol{\theta}-\boldsymbol{\theta}_n(d)) \quad (1)$$

where $p(\tau)$ denotes the transmitted pulse – the PN codeword after matched filtering – from a unity-gain omnidirectional antenna, δ denotes the Dirac delta function, and the parameter B denotes the bandwidth in GHz units defined with respect to the actual 2 GHz bandwidth used for the measurements. The spatial CIR is equivalent to what a RX (also with a unity-gain omnidirectional antenna) would detect at d, *i.e.,* N copies of the transmitted pulse, each corresponding to a different path n scaled by complex amplitude $\alpha_n(d)$ and arriving with delay $\tau_n(d)$ and at angle $\boldsymbol{\theta}_n(d)$.

To visualize the dependence on bandwidth, Fig. 3(a) shows the 2 GHz transmitted pulse $p(\tau)$ resampled to provide pulses corresponding to 10 MHz, 50 MHz, 100 MHz, and 500MHz bandwidths as well. The CIR of the illustrative channel steered towards the Whiteboard is shown in Fig. 3(b) for the five bandwidths. As the bandwidth widens, the width of the pulse – or equivalently the width of the delay bin – narrows. Hence fewer paths are detected per delay bin. This was also observed in measurements in [23], [32].

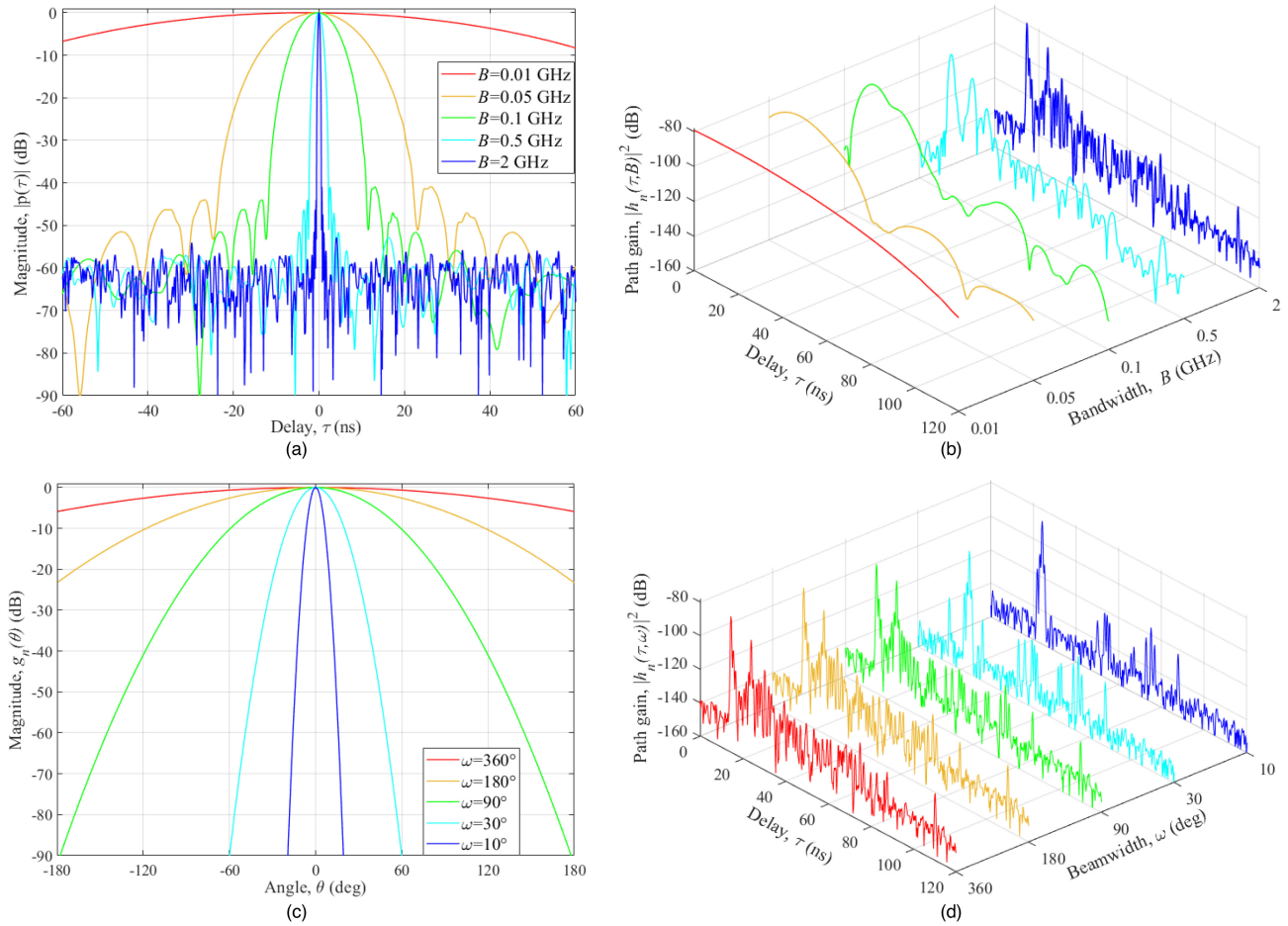

FIGURE 3. Beamwidth- and bandwidth-dependence of an illustrative channel steered towards the Whiteboard scatterer in a Laboratory scenario. (a) Bandwidth-dependent transmitted pulse and (b) corresponding bandwidth-dependent CIR: more paths are resolvable as bandwidth widens. (c) Beamwidth-dependent antenna pattern and (d) corresponding beamwidth-dependent CIR: less paths are detected as beamwidth narrows.

C. BEAMWIDTH DEPENDENCE

Finally, the bandwidth-dependent CIR in (1) was extended to make it beamwidth dependent as well, by applying synthetic horns with variable beamwidth at both ends. The synthetic horns were steered towards $\boldsymbol{\theta}_n(d)$, the double-directional angle of persistent path n. As mentioned earlier, since the angle is a function of d, alignment is maintained with the persistent path as the RX moves along the rail. The synthetic horn has a 3D Gaussian pattern (as our scalar feed horns) with unity gain and half-power beamwidth defined in degrees by parameter ω [33]:

$$g_n(\boldsymbol{\theta};\omega) = e^{-\left(\frac{\boldsymbol{\theta}-\boldsymbol{\theta}_n(d)}{0.6\ \omega}\right)^2} \tag{2}$$

The Gaussian beam pattern is applied to (1) to reconstruct the beamwidth- and bandwidth-dependent CIR of the channel steered towards persistent path n as

$$h_n(d,\tau;\omega,B) = \int_{[0,0,0,0]}^{[2\pi,\pi,2\pi,\pi]} g_n(\boldsymbol{\theta};\omega)\cdot h(d,\tau,\boldsymbol{\theta};B)d\boldsymbol{\theta}. \tag{3}$$

The double-directional gain $g_n(\boldsymbol{\theta};\omega)$ effectively attenuates paths in proportion to their angular separation from $\boldsymbol{\theta}_n(d)$, where ω controls the roll-off. The paths are then integrated over all angles. Fig. 3(c) shows the Gaussian pattern of the synthetic horn for 360°, 180°, 90°, 30°, and 10° beamwidths and Fig. 3(d) shows the corresponding CIR steered towards the whiteboard. Narrowing the beam admits fewer and fewer paths into the channel.

IV. ANALYSIS OF WIDE-SENSE STATIONARITY

In this section, the beamwidth and bandwidth of the CIRs are varied to determine the crossover points when the channel transitions from WSS to non-WSS. Then the statistics of the crossover beamwidths and bandwidths are compiled over all the measured channels for comprehensive analysis.

A. CROSSOVER BEAMWIDTH AND CROSSOVER BANDWIDTH

The wide-sense stationarity of the channel is determined by analyzing how its response varies along the rail. The channel response per displacement is computed from (3) by summing the power over all the peaks in the CIR, expressed as

$$r_n(d;\omega,B) = \sum_{\tau=\tau_{\text{peak}}} |h_n(d,\tau;\omega,B)|^2. \tag{4}$$

We only sum over the peaks in the CIR rather than over the whole CIR since the channel is sparse and so the summation

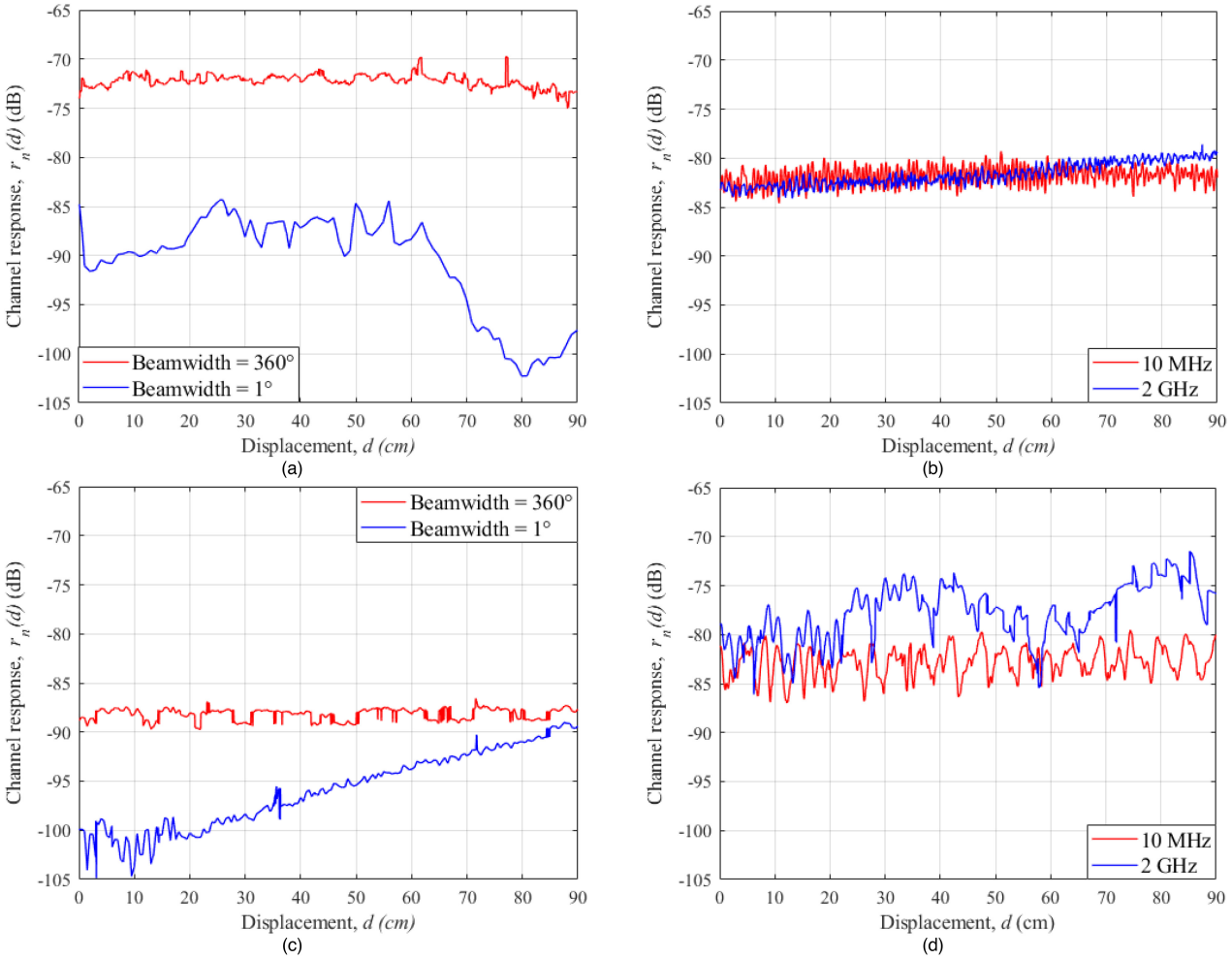

FIGURE 4. Variation in the channel response along the rail for illustrative indoor and outdoor channels, steered towards the Whiteboard in the Laboratory (a,b) and towards the Northeast building in the Courtyard (c,d). (a,c) At 360° beamwidth, the mean path gain is displacement invariant (WSS) whereas at 1° beamwidth it is not (non-WSS). (b,d) At 10 MHz bandwidth, the mean path gain is displacement invariant (WSS) whereas at 2 GHz bandwidth it is not (non-WSS).

would otherwise be dominated by noise samples, not channel samples. The peaks are identified by the *findpeaks* algorithm in MATLAB® [34], which defines a peak as a data sample that is larger than its two neighboring samples.

When the antenna beamwidth is wide – analogously, when the channel bandwidth is narrow – each peak is the complex summation over many paths, averaging out any displacement-specific characteristics and resulting in a WSS channel. Consider again the CIR of the channel steered towards the Whiteboard in Fig. 3(d). Fig. 4(a) shows the corresponding response as it varies along the rail. For 360° beamwidth, the local variation in the response is about the same across the whole rail; the channel is in fact WSS. At the other extrema, when the beamwidth is reduced to 1°, few paths sum per peak, lending to deep fades towards the end of the rail compared to the beginning; the channel is in fact non-WSS. The analogous comparison for the Whiteboard channel is shown in Fig. 4(b): the local variation in the response is about the same across the whole rail at 10 MHz, whereas at 2 GHz the mean path gain steadily increases. Curves for an illustrative outdoor channel steered towards the Northeast building in the Courtyard are also shown, in Fig. 4(c) and Fig. 4(d).

If the channel is WSS,[2] its mean $\mu_n(d)$ and autocorrelation $R_n(d, \Delta d)$ are displacement invariant, *i.e.*, $\mu_n(d) = \mu_n$ and $R_n(d, \Delta d) = R_n(\Delta d)$. In practice, the mean can be approximated by the sample mean

$$\mu_n(d) = \mathbb{E}[r_n(d)] \tag{5a}$$

$$\approx \frac{1}{2\epsilon} \int_{d-\epsilon}^{d+\epsilon} r_n(\tilde{d}) d\tilde{d} \tag{5b}$$

where the expectation is taken over a moving window of size 2ϵ. Likewise, the autocorrelation can be approximated

2. The function $r_n(d)$ defined in (4) and based on absolute values of the peaks of the channel response is not the channel impulse response itself. Therefore, even when its mean and autocorrelation, as defined in (5) and (6) respectively, are displacement invariant, the channel is still not guaranteed to be perfectly WSS following the definitions of wide-sense stationarity in the literature. On the other hand, if the channel is fully WSS, then the mean and autocorrelation of $r_n(d)$ will be always displacement invariant. Thus, our test is a sound indication of the WSS property while not being perfectly rigorous.

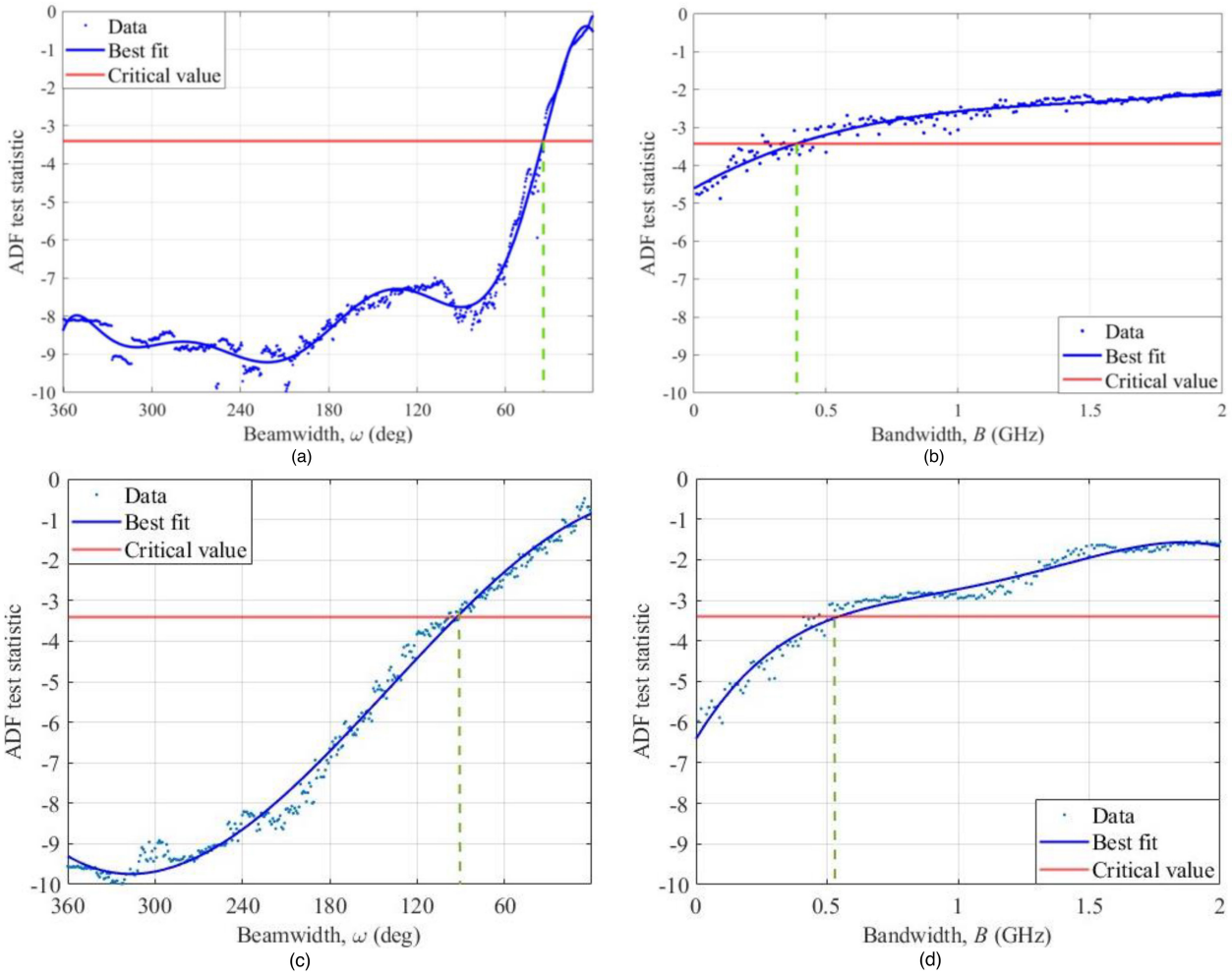

FIGURE 5. ADF test statistic as a function of beamwidth, from 360° to 1° in 1° steps, showing the crossover beamwidth when channel transitions from WSS to non-WSS (when the best fit curve to the data rises above the critical value): (a) 34° for the illustrative indoor channel and (c) 93° for the illustrative outdoor channel. ADF test statistic as a function of bandwidth, from 10 MHz to 2 GHz in 10 MHz steps, showing the crossover bandwidth when channel transitions from WSS to non-WSS: (b) 380 MHz for the indoor channel and (d) 541 MHz for the outdoor channel.

by the sample autocorrelation

$$R_n(d, \Delta d) = \mathbb{E}[r_n(d) \cdot r_n(d + \Delta d)] \tag{6a}$$

$$\approx \frac{1}{2\epsilon} \int_{d-\epsilon}^{d+\epsilon} r_n(\widetilde{d}) \cdot r_n(\widetilde{d} + \Delta d) d\widetilde{d}. \tag{6b}$$

And in practice it could be determined whether the channel is WSS by observing if the sample mean and the sample autocorrelation vary over displacement less than some thresholds. But the determination would be heavily influenced by the threshold values selected as well as the window size, the number of displacement samples in the channel response, etc.

Rather, we resort to the well-recognized Augmented Dickey-Fuller test [35] to determine whether the channel is WSS. The test models the channel response as the following stochastic process

$$r_n(\Delta d) = \alpha + \beta d + \gamma r_n(d) + \upsilon_1 r_n(\Delta d_1) + \cdots + \upsilon_p r_n(\Delta d_p) + w(d), \tag{7}$$

where the differential response $r_n(\Delta d) = r_n(d) - r_n(d-1)$ at d and the p lagged differential responses at $d-1, \ldots, d-p$ are given from (4), and $w(d)$ is white noise. If the process contains a zero root ($\gamma = 0$), then the associated term $r_n(d)$ – the only term that varies with displacement d whereas all the other terms vary with relative displacement Δd – does not affect the process; it follows that the process is displacement invariant and so the channel can be deemed WSS; it is otherwise deemed non-WSS ($\gamma < 0$). In practice, the process is considered to contain a zero root if the *ADF test statistic* is higher than a critical value. The ADF statistic is computed from the channel response through a lengthy algorithm (whose description is beyond the scope of this paper) and depends on the number of displacement samples in the response and the confidence level, among other factors. Here we use a confidence level of 99%.

Fig. 5(a) shows the ADF test statistic of the channel steered towards the Whiteboard as a function of beamwidth, from 360° down to 1° in 1° steps (the bandwidth is set to the channel sounder's 2 GHz value). The best fit curve over the data is also shown. The red line indicates the critical value.

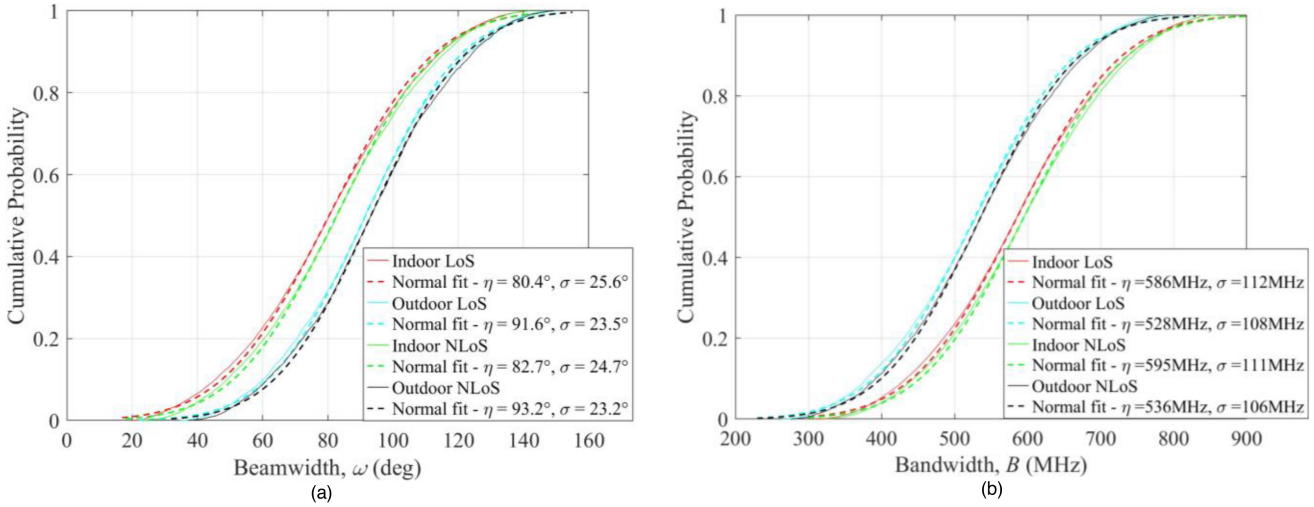

FIGURE 6. Cumulative distribution functions CDFs of (a) crossover beamwidth and (b) crossover bandwidth compiled across Indoor LoS, Outdoor LoS, Indoor NLoS, and Outdoor NLoS scenarios. The measurement CDFs are shown as solid lines while the best fit Normal CDFs are showed as dashed lines with associated mean (η) and standard deviation (σ) parameters.

At 360°, the channel is WSS but, as the beamwidth is narrowed, it gradually transitions to non-WSS at 34° crossover beamwidth, where the best fit curve rises above the critical value. Analogously, Fig. 5(b) shows the test statistic as a function of bandwidth, from 10 MHz to 2 GHz in 10 MHz steps (the beamwidth is set to the 360° azimuth FoV of the channel sounder). At 10 MHz, the channel is WSS but, as the bandwidth is widened, it gradually transitions to non-WSS at 380 MHz crossover bandwidth. Curves for the illustrative outdoor channel steered towards the Northeast building in the Courtyard are also shown, in Fig. 5(c) and Fig. 5(d).

It is important to note, as pointed out in Section III-C, that here we consider the case for when the TX and RX beams are realigned with the persistent path as the RX is displaced along the rail. This corresponds to the most favorable case for wide-sense stationarity. Misalignment causes the channel response to vary even more with displacement along the rail, the case we consider in [36].

B. STATISTICAL ANALYSIS

For each of the 88 channels, the beamwidth and bandwidth were varied jointly down from 360° and up to 2 GHz respectively to determine the crossover points. Copulas were used to assess the joint dependence of the beamwidth and bandwidth crossover points. Copulas are used to provide a dependence structure between random variables along with the corresponding multivariate distribution [37]. However, the resulting copulas in our case showed weak dependence throughout the entirety of the data set. Ultimately it was determined that the beamwidth and bandwidth crossover points can be modeled independently.

Accordingly, cumulative distribution functions (CDFs) of the crossover beamwidth are shown in Fig. 6(a). For general representation of indoor and outdoor environments, CDFs were compiled over all persistent paths in Laboratory, Lobby, and Lecture Room and over all persistent paths in the Pathway and Courtyard, respectively. Because the measurements were conducted in LoS conditions, the green and red plots with solid lines are labeled as Indoor LoS and Outdoor LoS respectively. Next, the best fit distributions to the measurements were found to be Normal CDFs, superimposed in the same colors as the measurement CDFs but with dotted lines, with the average (η) and standard deviation (σ) of the fit parameters in the legend. Finally, to emulate non-LoS (NLoS) conditions, the LoS path – easily identifiable as the first and strongest path – was removed from each of the CIRs in (1) and the CDFs were recompiled and refit, again with the best fit found to be Normal CDFs, and are also shown in Fig. 6(a), in green and black for the indoor and outdoor environments respectively. The same analysis was conducted for varying bandwidth and the analogous results are shown in Fig. 6(b).

Kolmogorov-Smirnov (KS) test was used to determine the best fit distribution in Fig. 6(a) and 6(b) [38]. The KS stat – a value between 0 and 1 indicating the fit error between two distributions, along with the corresponding p-value were obtained for each CDF. All KS stat value were below 0.0192, indicating a good fit. The corresponding p-values in all cases were above the 5% significance level, indicating acceptance of the null hypothesis that both samples are from the same distribution.

The mean crossover beamwidth in LoS for the indoor and outdoor environment are 80.4° and 91.6° respectively. The outdoor value is notably higher because it is a sparser environment; so the channel transitions to non-WSS earlier when decreasing beamwidth from 360°. The mean crossover bandwidth in LoS for the indoor and outdoor environments is 586 MHz and 528 MHz respectively. The outdoor value is notably lower for the same reason; so the channel transitions later to non-WSS when increasing bandwidth to 2 GHz.

In NLoS conditions there is only one less path than in LoS conditions, but since it is the strongest path, it does

affect the comprehensive results. As expected, when decreasing beamwidth from 360°, the channel transitions earlier to non-WSS with respect to LoS, but only about 2° earlier for both indoor and outdoor environments. Analogously, when increasing the bandwidth to 2 GHz, the channel does transition later to non-WSS, but only about 8 MHz later for both the indoor and outdoor environments.

V. CONCLUSION

When a wireless propagation channel is said wide-sense stationary (WSS), the mean and autocorrelation of its small-scale fading are position invariant. Because this property is supported by measurement-based validation in the microwave bands, it was assumed to hold true in the millimeter-wave bands as well… without validation. To fill that void, in this paper we conduct a comprehensive evaluation of the wide-sense stationarity of 88 channels measured with our 60 GHz channel sounder in three indoor and two outdoor environments. We found that at narrow beamwidths – below 80.4° for indoor and 91.6° for outdoor – the channel transitions from WSS to non-WSS; analogously, we found that at wide bandwidths – above 586 MHz for indoor and 528 MHz for outdoor – the channel transitions from WSS to non-WSS.

REFERENCES

[1] M. Pätzold, *Mobile Radio Channels*. New York, NY, USA: Wiley, 2011.

[2] J. D. Parsons and P. J. D. Parsons, *The Mobile Radio Propagation Channel*, vol. 2. New York, NY, USA: Wiley, 2000.

[3] P. Bello, "Characterization of randomly time-variant linear channels," *IEEE Trans. Commun. Syst.*, vol. 11, no. 4, pp. 360–393, Dec. 1963, doi: 10.1109/TCOM.1963.1088793.

[4] N. Iqbal et al., "Multipath cluster fading statistics and modeling in millimeter-wave radio channels," *IEEE Trans. Antennas Propag.*, vol. 67, no. 4, pp. 2622–2632, Apr. 2019, doi: 10.1109/TAP.2019.2894277.

[5] N. Iqbal et al., "Investigating validity of wide-sense stationary assumption in millimeter wave radio channels," *IEEE Access*, vol. 7, pp. 180073–180082, 2019, doi: 10.1109/ACCESS.2019.2957949.

[6] M. K. Samimi, G. R. MacCartney, S. Sun, and T. S. Rappaport, "28 GHz millimeter-wave ultrawideband small-scale fading models in wireless channels," in *Proc. IEEE 83rd Veh. Technol. Conf. (VTC Spring)*, Nanjing, China, 2016, pp. 1–6, doi: 10.1109/VTCSpring.2016.7503970.

[7] M. Kim, R. Takahashi, and H. Tsukada, "Millimeter-wave cluster channel model validation from small-scale fading measurements," in *Proc. IEEE 33rd Annu. Int. Symp. Pers. Indoor Mobile Radio Commun. (PIMRC)*, Kyoto, Japan, 2022, pp. 1–5, doi: 10.1109/PIMRC54779.2022.9977991.

[8] D. Cassioli, M. Z. Win, and A. F. Molisch, "The ultra-wide bandwidth indoor channel: From statistical model to simulations," *IEEE J. Sel. Areas Commun.*, vol. 20, no. 6, pp. 1247–1257, Aug. 2002, doi: 10.1109/JSAC.2002.801228.

[9] D. S. Baum et al., "D5.4 final report on link level and system level channel models, v1.4," IST, Tallinn, Estonia, IST-2003–507581 WINNER, Nov. 2005.

[10] P. Kyösti et al., "WINNER II D1.1.2 v1.2 WINNER II channel models," IST, Tallinn, Estonia, IST-4-027756, 2007.

[11] L. M. Correia, Ed., *Wireless Flexible Personalized Communications–COST 259: European Co-Operation in Mobile Radio Research*. New York, NY, USA: Wiley, 2001.

[12] L. Liu et al., "The COST 2100 MIMO channel model.," *IEEE Wireless Commun.*, vol. 19, no. 6, pp. 92–99, Dec. 2012.

[13] A. Maltsev, "Channel modeling and characterization—MiWEBA," MiWEBA, Breitengüßbach, Germany, document deliverable 5.1 EU no. FP7-ICT-608637, 2014.

[14] V. Nurmela et al., "METIS channel models," FP7 METIS, Stockholm, Sweden, document no. ICT-317669-METIS/D1, 2015.

[15] A. Maltsev, A. Pudeyev, A. Lomayev, and I. Bolotin, "Channel modeling in the next generation mmWave Wi-Fi: IEEE 802.11ay standard," in *Proc. 22nd Eur. Wireless Conf.*, May 2016, pp. 1–8.

[16] "Study on channel model for frequencies from 0.5 to 100 GHz," 3GPP, Sophia Antipolis, France, 3GPP TR 38.901 version 14.1.1 release 14, Jul. 2017.

[17] mmMAGIC, (May 2017), "Measurement results and final mmMAGIC channel models, H2020-ICT-671650-mmMAGIC/D2.2 v1.0," [Online]. Available: https://5g-mmmagic.eu/results/

[18] "Spatial channel model for multiple input multiple output (MIMO) simulations (release 16)," 3GPP, Sophia Antipolis, France, 3GPP TR 25.996, Jul. 2020.

[19] A. Maltsev et al., *Channel Models for 60 GHz WLAN Systems*, IEEE Standard 802.11–09/0334r8, 2010.

[20] J. Senic, C. Gentile, P. B. Papazian, K. A. Remley, and J.-K. Choi "Analysis of E-band path loss and propagation mechanisms in the indoor environment," *IEEE Trans. Antennas Propag.*, vol. 65, no. 12, pp. 6562–6573, Dec. 2017, doi: 10.1109/TAP.2017.2722876.

[21] W. Sloane et al., "Measurement-based analysis of millimeter-wave channel sparsity," *IEEE Antennas Wireless Propag. Lett.*, vol. 22, no. 4, pp. 784–788, Apr. 2023, doi: 10.1109/LAWP.2022.3225246.

[22] M. Ptzold and G. Rafiq, "Sparse multipath channels: Modelling, analysis, and simulation," in *Proc. IEEE PIMRC*, 2013, pp. 30–35, doi: 10.1109/PIMRC.2013.6666099.

[23] A. F. Molisch, "Ultrawideband propagation channels-theory, measurement, and modeling," *IEEE Trans. Veh. Technol.*, vol. 54, no. 5, pp. 1528–1545, Sep. 2005, doi: 10.1109/TVT.2005.856194.

[24] V. Va, J. Choi, and R. W. Heath, "The impact of beamwidth on temporal channel variation in vehicular channels and its implications," *IEEE Trans. Veh. Technol.*, vol. 66, no. 6, pp. 5014–5029, Jun. 2017, doi: 10.1109/TVT.2016.2622164.

[25] R. Sun et al., "Design and calibration of a double-directional 60 GHz channel sounder for multipath component tracking," in *Proc. 11th Eur. Conf. Antennas Propag. (EUCAP)*, 2017, doi: 10.23919/EuCAP.2017.7928270.

[26] K. Hausmair, K. Witrisal, P. Meissner, C. Steiner, and G. Kail, "SAGE algorithm for UWB channel parameter estimation," in *Proc. COST Manag. Committee Meeting*, 2010.

[27] P. B. Papazian et al., "Calibration of millimeter-wave channel sounders for super-resolution multipath component extraction," *Proc. EuCAP*, 2016, pp. 1–5, doi: 10.1109/EuCAP.2016.7481704.

[28] C. Gentile, P. B. Papazian, R. Sun, J. Senic, and J. Wang, "Quasi-deterministic channel model parameters for a data center at 60 GHz," *IEEE Antennas Wireless Propag. Lett.*, vol. 17, no. 5, pp. 808–812, May 2018, doi: 10.1109/LAWP.2018.2817066.

[29] C. Lai, R. Sun, C. Gentile, P. B. Papazian, J. Wang, and J. Senic, "Methodology for multipath-component tracking in millimeter-wave channel modeling," *IEEE Trans. Antennas Propag.*, vol. 67, no. 3, pp. 1826–1836, Mar. 2019, doi: 10.1109/TAP.2018.2888686.

[30] R. Charbonnier et al., "Calibration of ray-tracing with diffuse scattering against 28-GHz directional urban channel measurements," *IEEE Trans. Veh. Technol.*, vol. 69, no. 12, pp. 14264–14276, Dec. 2020.

[31] S. M. Bazaraa, J. J. Jarvis, and H. D. Sherali, *Linear Programming and Network Flows*. Hoboken, NJ, USA: Wiley, 2011.

[32] W. Q. Malik, B. Allen, and D. J. Edwards, "Fade depth scaling with channel bandwidth," *Electron. Lett.*, vol. 43, no. 24, pp. 1371–1372, Nov. 2007.

[33] R. Sun, P. B. Papazian, J. Senic, C. Gentile, and K. A. Remley, "Angle-and delay-dispersion characteristics in a hallway and lobby at 60 GHz," in *Proc. 12th Eur. Conf. Antennas Propag. (EuCAP)*, 2018, pp. 360–365, doi: 10.1049/cp.2018.0719.

[34] M. Llobera, "Building past landscape perception with gis: Understanding topographic prominence," *J. Archaeol. Sci.*, vol. 28, no. 9, pp. 1005–1014, 2001.

[35] D. A. Dickey and W. A. Fuller, "Distribution of the estimators for autoregressive time series with a unit root," *J. Amer. Statist. Assoc.*, vol. 74, no. 366, pp. 427–431, 1979.

[36] A. Hughes et al., "Measuring the impact of beamwidth on the correlation distance of 60 GHz indoor and outdoor channels," *IEEE Open J. Veh. Technol.*, vol. 2, pp. 180–193, 2021.
[37] G. Karaali, *Book Review: Encyclopedia of Mathematics and Society*. Washington, DC, USA: Math. Assoc. America, 2013.
[38] F. J. Massey, "The Kolmogorov-Smirnov test for goodness of fit," *J. Amer. Statist. Assoc.*, vol. 46, no. 253, pp. 68–78, 1951.

ANMOL BHARDWAJ received the B.A.Sc. and M.A.Sc. degrees in electrical and computer engineering from the University of British Columbia, Vancouver, Canada. From October 2017 to December 2018 and then since November 2019, he has been working as an Electromagnetics Researcher with the Radio Access and Propagation Metrology Group, National Institute of Standards and Technology. His research interests include channel propagation modeling and measurements.

JACK CHUANG received the Ph.D. degree from The Pennsylvania State University, State College, PA, USA, in 2008, where he was a Graduate Research Assistant with Communications and Space Sciences Laboratory. Then, he worked with BAE Systems, Merrimack, NH, USA, in electronic warfare and Cisco Systems, Richfield, OH, USA, in spectrum sharing. He is currently with the Communication Technology Laboratory, NIST, Gaithersburg, MD, USA, developing 5G mmWave channel sounders.

CAMILLO GENTILE (Member, IEEE) received the Ph.D. degree in electrical engineering from The Pennsylvania State University in 2001. He joined the National Institute of Standards and Technology, Washington, DC, USA, in 2001, where he is currently leading the Radio Access and Propagation Metrology Group and the NextG Channel Measurement and Modeling Project with Communications Technology Laboratory. He has authored over 100 peer-reviewed journals and conference papers, a book on geolocation techniques, and a book on millimeter-wave and sub-terahertz channel propagation modeling. His current interests include channel modeling and physical-layer modeling for 5G and 6G wireless systems.

CHIEHPING LAI received the M.S. and Ph.D. degrees in electrical engineering from The Pennsylvania State University, University Park, in 2004 and 2007, respectively. He is an Electronics Engineer with the Communications Technology Laboratory, NIST. He is interested in mmwave systems, tracking algorithms, and data processing.